Theory and Experiments of Transport at Channel Microband Electrodes under Laminar Flows. 2. Electrochemical Regimes at Double Microband Assemblies under Steady State

Christian Amatore, Nicolas da Mota, Célia Lemmer, Cécile Pebay, Catherine Sella, Laurent Thouin

▶ **To cite this version:**

Christian Amatore, Nicolas da Mota, Célia Lemmer, Cécile Pebay, Catherine Sella, et al.. Theory and Experiments of Transport at Channel Microband Electrodes under Laminar Flows. 2. Electrochemical Regimes at Double Microband Assemblies under Steady State. Analytical Chemistry, 2008, 80 (24), pp.9483-9490. 10.1021/ac801605v . hal-00433376

HAL Id: hal-00433376
https://hal.science/hal-00433376

Submitted on 19 Nov 2009

HAL is a multi-disciplinary open access archive for the deposit and dissemination of scientific research documents, whether they are published or not. The documents may come from teaching and research institutions in France or abroad, or from public or private research centers.

L'archive ouverte pluridisciplinaire **HAL**, est destinée au dépôt et à la diffusion de documents scientifiques de niveau recherche, publiés ou non, émanant des établissements d'enseignement et de recherche français ou étrangers, des laboratoires publics ou privés.

Theory and Experiments of Transport at Channel Microband Electrodes under Laminar Flows. 2. Electrochemical Regimes at Double Microband Assemblies under Steady-State

Christian Amatore,* Nicolas Da Mota, Célia Lemmer, Cécile Pebay, Catherine Sella and Laurent Thouin*

Ecole Normale Supérieure, Département de Chimie, UMR CNRS-ENS-UPMC 8640 " Pasteur ", 24 rue Lhomond, F-75231 Paris Cedex 05, France

ABSTRACT

The development of any particular analytical or preparative applications using electrochemical techniques in microfluidic devices requires integration of microelectrodes. This involves detailed predictions for optimizing the design of devices and selecting the best hydrodynamic conditions. For this purpose, we undertook a series of works aimed to a precise investigation of mass transport near electrodes with focus on analytical measurements. Part I of this series (Anal. Chem. 2007, 79, 8502-8510) evaluated the common case of a single microband electrode embedded within a microchannel under laminar flow. The present work (Part 2) investigated the case of a pair of microband electrodes operating either in generator-generator or generator-collector modes. The influence of the confining effect and flow velocity on the amperometric responses was examined on the basis of numerical simulations under steady-state regime. Several situations were identified, each of them corresponding to specific interactions taking place between the electrodes. Related conditions were extracted in order to establish a zone diagram describing all the situations. These predictions were systematically validated by experimental measurements. The results show that amperometric detections within microchannels can be performed at dual electrodes with higher analytical performances than at single ones.

Keywords: Microchannel; Microelectrode; Microfluidic; Mass transport; Hydrodynamics; Concentration profile.

* To whom correspondence should be addressed. E-mail: christian.amatore@ens.fr and laurent.thouin@ens.fr

INTRODUCTION

Electrochemistry is very adapted to perform analytical detections within microfluidic devices.[1-3] The standard photolithographic techniques have brought great contributions to miniaturizations and they have facilitated simultaneously implementation of electrodes in microdevices. It is now possible to carry out *in situ* electrochemical measurements in very small volumes using portable instrumentations.

Electrochemistry offers several advantages in comparison to other analytical techniques due to their kinetic character. The signal-to-noise responses of electrodes are proportional to the concentration of the electroactive materials and not to quantities as it occurs for other analytical measurements. This is an important issue when quantity may be decreased due to the use of microvolumes. Amperometric detections can be performed without labeling the species while keeping low sensibilities. Higher performances can be achieved by employing arrays of microelectrodes. Mass transport is increased and redox cycling can be established between electrodes.[4-7] In parallel, many strategies can be explored according to the type of detection considered. Procedures have been defined either to eliminate interfering species prior to subsequent analytical steps,[8-10] to generate titrating species for indirect detections,[11-13] or to tag molecules for mass spectrometric analysis.[14, 15] Apart from these applications, dual electrode assemblies offer many other advantages.[16]. On the one hand, spatially resolved chemical reactions can be induced to generate *in situ* electrochemiluminescence[17, 18] or to produce highly instable intermediates during electrosynthesis.[19-21] On the other hand, this dual configuration allows the monitoring of flow velocities in microfluidic channels,[22-28] evaluation of diffusion coefficients,[29-31] studies of homogeneous or heterogeneous kinetics,[11, 29, 32-36] and analyses of complex media.[37, 38]

From an analytical point of view, we demonstrated conceptually the benefit of using several electrodes instead of a single one to detect and analyze the composition of injected samples.[39] For a full quantitative application of the above potentialities, mass transport in microchannel must be fully and quantitatively mastered if any optimization of an electrochemical detection is required. Mass transport at dual channel electrodes has been already extensively investigated on the basis of theoretical and numerical simulations.[11, 22, 26, 29, 32, 34, 35, 40-46] However, most of these studies were devoted to the investigation of purely electrochemical problems that microfluidic environment could solve or to investigate local hydrodynamics of flow. The purpose of this work is rather to exploit steady-state electrochemical components of a dual electrode configuration to define ultimately the pre-required conditions of an optimized electrochemical detection of an analyte flowing in a microchannel. This work is then a continuation of a first study investigating the electrochemical properties of a single microchannel electrode under laminar flow.[47]

In the following, a pair of independent microelectrodes (E1 and E2) embedded in the wall of a rectangular microchannel is considered and their individual amperometric responses are discussed as a

function of their polarization and of the device geometry or flow velocity. Two operating modes are examined according to the fact that the electrodes can be biased respectively as generator-generator (GG mode) and generator-collector (GC mode). In GG mode, both electrodes are probing the substrate in the microchannel and the advantages of this mode versus a single electrode will be discussed. In GC mode, the electrode E2 located downstream is collecting the product generated by E1. According to the gap distance separating the electrodes and the flow velocity in the microchannel, different types of interaction can take place between the electrodes performing in either mode. The related conditions leading to such situations will be extracted and examined in view of their analytical meaning and use. For that purpose, the electrochemical responses were simulated numerically and compared to experiments performed at two microband electrodes integrated within microchannels. An aqueous solution of ferrocene methanol was continuously transferred under pressure-driven flow.

PRINCIPLE

As mentioned previously, the device consists of two parallel microband electrodes placed on the floor of a rectangular microchannel (Figure 1A). w_1 and w_2 are respectively the widths of the upstream E1 and downstream E2 electrodes, g the gap distance and h the microchannel height. The length of both electrodes corresponds to the microchannel width L with L being much larger than w_1 and w_2. The formulation of problem is thus reduced to a two-dimensional system as described in Figure 1B.[48]
The electrochemical reaction is supposed to be reversible:

$$\mathrm{A} + n\,\mathrm{e}^- \rightleftarrows \mathrm{B} \qquad (1)$$

where A is the reactant and B the product. n being positive (reduction) or negative (oxidation) features the number of electron exchanged during the electrochemical reaction. Diffusion coefficients of the two electroactive species are supposed identical and equal to D as it occurs in most applications in classical liquids. Mass transport is the rate determining step and is governed inside the microchannel by diffusion and convection:

$$\frac{\partial c}{\partial t} = D\left(\frac{\partial^2 c}{\partial x^2} + \frac{\partial^2 c}{\partial y^2}\right) - u_x(y)\frac{\partial c}{\partial x} \qquad (2)$$

Because of mass conservation only one species (A or B) needs to be examined. Diffusion occurs along the x and y-axis whereas convection operates exclusively parallel to the x-axis. $u_x(y)$ is the flow velocity supposed to be parabolic across the microchannel section:

$$u_x(y) = 6u_{\mathrm{av}}\frac{y}{h}\left(1 - \frac{y}{h}\right) \qquad (3)$$

u_{av} is the average flow velocity with $u_{\mathrm{av}} = 2u_{\mathrm{max}} / 3$ where u_{max} is the maximum flow velocity at $y = h / 2$. To offer a large generality to the resolution of the problem, dimensionless parameters were

introduced. Geometrical parameters are normalized by the microchannel height h with $X = x / h$, $Y = y / h$, $W_1 = w_1 / h$, $W_2 = w_2 / h$ and $G = g / h$. Concentrations are normalized with respect to the bulk concentration c^0 of the reactant A initially present in the input solution as $C = c / c^0$. Note that B is supposed to be absent in the input solution. The time scale is $\tau = Dt / h^2$ where h^2 / D represent the time for diffusion to extend vertically across the channel. The average flow velocity is introduced through a Peclet number such as:

$$Pe = \frac{u_{av} h}{D} \tag{4}$$

With these dimensionless notations, eqs (2) and (3) become respectively:

$$\frac{\partial C}{\partial \tau} = \left(\frac{\partial^2 C}{\partial X^2} + \frac{\partial^2 C}{\partial Y^2} \right) - V_x(Y) \frac{\partial C}{\partial X} \tag{5}$$

and

$$V_x(Y) = \frac{u_x(y) h}{D} = 6 \; Pe \; Y(1 - Y) \tag{6}$$

Eq (5) is solved numerically by finite differences when steady-state conditions prevail (*i.e.*, when $\partial C / \partial \tau = 0$). This is performed in association with the following boundary conditions:

$C = 1$ at the microchannel entrance (input solution)

$C = 0$ at electrodes operating as generator (*i.e.*, biased on the plateau of the A/B wave)

$C = 1$ at electrodes operating as collector (*i.e.*, biased on the plateau of the B/A wave)

$\frac{\partial C}{\partial Y} = 0$ at insulating surfaces

Finally, we imposed the origin of the X-axis arbitrarily at the downstream edge of E1 (Figure 1B). Then the dimensionless currents ψ flowing at each electrode were calculated such as:

$$\text{E1: } \Psi_{g1} = \frac{i_{g1}}{nFLDc^\circ} = \int_{-W_1}^{0} \frac{\partial C}{\partial Y}\Big|_{Y=0} dX \tag{7}$$

$$\text{E2 (GG mode) : } \Psi_{g2} = \frac{i_{g2}}{nFLDc^\circ} = \int_{G}^{W_2+G} \frac{\partial C}{\partial Y}\Big|_{Y=0} dX \tag{8}$$

$$\text{E2 (GC mode) : } \Psi_{c2} = -\frac{i_{c2}}{nFLDc^\circ} = -\int_{G}^{W_2+G} \frac{\partial C}{\partial Y}\Big|_{Y=0} dX \tag{9}$$

ψ_{g1} (or i_{g1}) is the current of electrode E1 operating as generator. ψ_{g2} and ψ_{c2} (or i_{g2} and i_{c2}) are the currents of electrode E2 operating as a generator or collector depending on the mode of operation (GG or GC mode) of the assembly. F is the Faraday.

EXPERIMENTAL SECTION

The fabrication of the devices was performed as already reported.[25, 47] They consisted of two separate parts assembled ultimately together. The top one, made in polydimethylsiloxane (PDMS), comprises a series of independent channels with their reservoir elements. The channel floor was a glass substrate on which platinum or gold microband electrodes were patterned. As the linear microchannels were placed perpendicularly to the microbands, the effective microband lengths were delimited by the microchannels width ($L \sim 500$ μm) and the volume of solution flowing above the microband was restricted by the microchannel heigth ($h \sim 18$ μm). All the characteristic dimensions (w_1, w_2, g, h, L) were checked optically before use.

During one experiment, only one microchannel was filled with solution, the others remaining empty. The liquid flow in the microchannel was pressure driven using either a syringe pump (Harvard Apparatus, type 11 Pico Plus) or a controlled gas flux (argon) over the input reservoir of solution. The values of average flow velocities inside the microchannel were systematically monitored *in situ* by direct measurements following a procedure previously described.[25, 28] This allowed to vary precisely Peclet numbers between 10 and 400.

All electrochemical experiments were performed at room temperature using a home made multipotentiostat adapted from an original design.[49] The counter-electrode (CE) consisted of one large platinum or gold band electrode ($w \sim 500$ μm) located downstream far after the working electrodes (E1 and E2) whereas the platinum or gold band used as pseudo-reference electrode (REF) was located upstream. The two working electrodes E1 and E2 were biased independently at constant potentials and their currents monitored separately. The aqueous solution was 1mM ferrocene methanol (97% Acros organics) in 0.1 M potassium chloride as supporting electrolyte to ensure the absence of any migration contribution. This solution was previously degassed with argon prior to any experiments. The electrode potential was set at +0.4 V/REF when operating as generator or -0.1 V/REF when operating as collector (E2 only).

Amperometric responses were monitored after sufficiently long time durations to ensure that the steady-state limiting currents were always reached. The diffusion coefficient of ferrocene methanol was measured independently and was equal to $D = (7.6 \pm 0.4)\ 10^{-6}$ cm^2s^{-1}.

Numerical simulations were performed using FEMLAB software (Comsol) controlled by a MATLAB interface (Mathworks).

RESULTS AND DISCUSSION

Influence of the geometrical and hydrodynamic parameters. According to the device geometry (W_1, W_2, G) and flow velocity (Pe), several limiting situations can be distinguished based on the dependence of steady-state currents monitored at the two electrodes and concentration profiles

established within the microchannel. Each situation depends on the nature or kind of interactions involved between the electrodes. The following approach was developed to define criteria for evaluating how the two electrodes may interact.

Two situations are illustrated in Figures 2AB as a function of the geometrical parameters and *Pe* for a pair of electrodes operated in GG and GC modes. According to the flow velocity, after passing beyond E1, the flow composition across the microchannel can be homogeneous (Figure 2A) or inhomogeneous (Figure 2B) before reaching E2. This is more quantitatively characterized upon plotting related concentration vertical profiles across the microchannel (*i.e.*, versus *Y*-axis) close to the upstream edge of E2 (Figures 2D). In both situations, E2 response depends on the performance of E1 whatever the prevailing situation. However, distinction can be made whether E2 is probing locally a homogeneous solution (Figure 2A) or detecting a concentration gradient (Figure 2B) produced by E1. This method allows two types of interactions to be characterized when sufficiently high flow velocities are applied. In the following, they are defined respectively as sequential (Figure 2A) and coupling (Figure 2B) regimes. These two situations arise for specific geometries (W_1, W_2, G) and flow velocities (*Pe*) as it will be disclosed below. Note that in both cases, E_1 is not influenced by E2 so that it operates like a single electrode in a microchannel.[47]

A third situation illustrated in Figure 2C occurs at a relatively low flow velocity whatever the GG and GC modes. It corresponds to conditions such as diffusion prevails sufficiently over convection to proceed backward against the flow. As a consequence, concentration gradients generated by E2 interpenetrate with those of E1 leading to stronger interactions between electrodes. This situation is defined as the cross-talk regime.[50, 51] In contrast to the two previous ones (Figures 2AB), E1 currents are now influenced by the activity of E2.

These three regimes and their transitions will be established quantitatively in the following.

Sequential regimes. As mentioned above, under such situation, E1 and E2 perform within a flow of homogeneous compositions so that their current responses are characteristic of electrodes operating alone in microchannels (*i.e.*, single electrodes). The homogeneous concentration C_h reached locally in between the electrodes is imposed by the performance of E1 and current at E2 is proportional to that at E1 times C_h (GG mode) or 1-C_h (GC mode). For example, when both electrodes have the same width, whatever the hydrodynamic flow regime, one has:

$$\frac{\Psi_{g2}}{\Psi_{g1}} = C_h \tag{10}$$

and:

$$\frac{\Psi_{c2}}{\Psi_{g1}} = 1 - C_h \tag{11}$$

Combination of eqs (10) and (11) gives a simple relation between ψ_{g2} / ψ_{g1} and ψ_{c2} / ψ_{g1}:

$$\frac{\Psi_{c2}}{\Psi_{g1}} = 1 - \frac{\Psi_{g2}}{\Psi_{g1}} \tag{12}$$

On the other hand, we established before that: [47]

$$C_h = 1 - \frac{\Psi_{g1}}{Pe} \tag{13}$$

where C_h is a function of W/Pe. Hence, when $W_1 = W_2 = W$, ψ_{g2} / ψ_{g1} (eq (10)) or ψ_{c2} / ψ_{g1} (eq (11)) depend only on this parameter W/Pe as shown in Figure 3. In this figure, zones I, II and III describe the different hydrodynamic regimes taking place at the electrodes as a function of (W,Pe) parameters.[47] Zone III corresponds to Levich regime, *i.e.*, when convection prevails over diffusion. Zone I is the thin-layer regime when the converse occurs and zone II represents the transition between the two others.

C_h can be then evaluated experimentally from E_1 and E_2 responses, either from ψ_{g1} (eq (13)), ψ_{g2} / ψ_{g1} (eq (10)), or ψ_{c2} / ψ_{g1} (eq (11)). Eq (13) was already checked experimentally in the case of single electrodes.[47] In the following, we thus focus on the use of eq (10). The current ratio ψ_{g2} / ψ_{g1} was evaluated at a pair of microband electrodes of identical widths ($W_1 = W_2 = W$) separated by a large gap. As illustrated by the data in Figure 3, a very good agreement was observed between experiments and theoretical predictions whatever the hydrodynamic regime imposed.

Note that analytical expressions of ψ_{g2} / ψ_{g1} and ψ_{c2} / ψ_{g1} can be established under Levich regime (zone III) in case of unequal electrode dimensions (see Appendix).

According to the device geometry and flow velocity, deviations from the variations of ψ_{g2} / ψ_{g1} or ψ_{c2} / ψ_{g1} predicted in Figure 3 for $W_1 = W_2 = W$ are thus indicative of other interactions taking place between electrodes such as the coupling (Figure 2B) or cross-talk regimes (Figure 2C).

Transition between sequential and coupling regimes. Figure 4 shows steady-state currents monitored at two electrodes of same widths ($W_1 = W_2 = 1$) operated either in GG (Figure 4A) or GC mode (Figure 4B). Geometries and flow velocities were selected so that only coupling and sequential regimes could occur while any possible cross-talk was eliminated (*see* below). This was ensured theoretically and experimentally by checking that under all conditions probed, currents at E1 were not influenced by the performance of E2 and that their variations were characteristic of single electrodes (Figures 4AB).[47] However, E2 responses show that two behaviors may be achieved according to G and Pe: (i) an independence on G that corresponds to the sequential regimes and (ii) some deviations from this common trend arising for particular values of (G,Pe) in cases of coupling. This is better quantified upon examining the variations of ψ_{c2} / ψ_{g1} as a function of W_2/Pe (Figure 4C). A detailed numerical

analysis with several W_1 and W_2 values showed that the transition between coupling and sequential regimes began only when G/Pe achieved specific values, $(G/Pe)_{trans}$, provided that the gap distance remains larger than the electrode widths (Figure 4D). Indeed, these data demonstrate that when $(W_1+W_2)/Pe < 0.25$ (*i.e.*, when convection prevailed on diffusion) transitions arose at $(G/Pe)_{trans} = 0.25$, whatever W_1 and W_2. The ratio G/Pe compares the average time needed by the solution to flow over the gap (*i.e.*, g / u_{av}) to the time needed by species to diffuse across the microchannel section (*i.e.*, h^2/D). A value of $G/Pe = 0.25$ thus corresponds the longest time needed by the flow to become again homogeneous after passing over E1. On the opposite, when $(W_1+W_2)/Pe > 0.25$, transitions began at lower G/Pe values. In these cases, diffusion may overcome more easily convection and the time required to observe such evolution resulted less. Change between these two behaviors arose approximately when $(W_1+W_2)/G \approx 1$. These results were checked experimentally using a pair of microband electrodes of equal widths operating either in GG or GC mode. As shown in Figures 4ABC, the data follow all the theoretical predictions within the accuracy of their experimental determinations.

Cross-talk regime. As described previously in full details,[47] diffusion may operate against the flow only when $WPe < 15$. Extended diffusion-convection layers may then develop laterally and vertically at the upstream edge of an electrode. In a two electrode configuration, a situation may thus happen when the two such large diffusion-convection layers overlap sufficiently for the operation at E2 to be fed back to E1 by diffusion (Figure 2C). In GC mode, ψ_{g1} increases due to the positive feedback of species between the electrodes (Figure 5B). In contrast, ψ_{g1} in GG mode decreases (negative feedback) due to the depletion of species due to the activity of E2 in the vicinity of E1 (Figure 5A). Because they critically depend on the ability of diffusion to creep back against the flows, these effects may occur only for small gap distances and low flow velocities. Accordingly, conditions for which cross-talk is observed are identical in both operating modes whenever the diffusion coefficients of the species (reactant A and product B) are similar. Variation of ψ_{g1} are particularly apparent in GC mode because the recycling of species taking place between electrodes (Figure 2C) gives rise to a characteristic current increase when E2 operates. A detailed analysis in this mode shows that amplification of Ψ_{g1} occurs when $GPe < 2$, whatever the electrode widths W_1 and W_2 (Figure 5C). Indeed, the product GPe compares the time needed by species to diffuse back over the gap (*i.e.*, g^2/D) to the average time needed by the solution to flow over the same gap (*i.e.*, g / u_{av}). No significant cross-talk may occur when GPe is large. Numerical analysis establishes that $GPe = 2$ is the upper limit required for a species to diffuse against the flow and reach E1. As cross-talk then takes place mostly between the closest edges of the two electrodes so that W_1 and W_2 have no major influence on this transition. These conditions correspond experimentally to very low flow velocities and for that reason were not

investigated here. However, the have been thoroughly documented for still solutions under conditions identical to those prevailing in microchannels.[25, 31, 51]

Zone diagram. Since the systems delineated above and their transitions involve many different parameters, they are not easily presented in a general situation. A convenient way to summarize them is by using a zone diagram. Such a diagram can be established on the basis of our above analyses. Indeed, provided that the gap is sufficiently large compared to that the electrode widths, the couple of G and Pe values determines all the operating conditions for which sequential, coupling and cross-talk regimes between electrodes may occur. In a (G,Pe) diagram, transitions evaluated above on current responses thus delimit three zones corresponding to each limiting case (Figure 6A). These results show generally that (i) sequential regime (zone Sq) occurs at high G provided that Pe is not too large; (ii) coupling (zone Cp) is set at high Pe provided that G is not too large and (iii) cross-talk (zone CT) is restricted to a range where G and Pe are low. However, a transition which has not been considered above at intermediate G and low Pe appears between sequential and cross-talk regimes. This new transition regime is apparent when considering concentrations in the form already presented in Figures 2DE. Since this occurs when Pe is not very large, we may reasonably restrict to the case where concentrations are homogeneous over a short range in between the electrodes (Figure 6B). Note that this situation differs from Figure 2E where the flow homogeneity between electrodes was attained over a wider range along the X-axis. The (G,Pe) coordinates associated to these specific limit are figured in the zone diagram by the dashed curve. Evidently, when G and Pe achieve much larger values this specific transition between sequential and coupling regimes tends asymptotically towards $G/Pe = 0.25$ *(i.e.,* for $G > 10$ and $Pe > 30$). At lower values, discrepancies appear delimitating a new zone (dashed area in Figure 6A). This zone is intermediate between the three others and thus stresses the notion that different descriptions of a complex system may be given depending on the selected criterion. Criteria based on current variations (Figures 4D and 5C) would allow only the zones delimited by the solid lines shown in Figure 6B so that the dashed area would not be recognized. Indeed, in this zone the current responses remain characteristic of the sequential regime whereas interactions between the electrodes (coupling or cross-talk) start to become already effective but show up only upon carefully analyzing concentration profiles. In these (G,Pe) conditions, the current responses are thus not indicative of the interactions arising between the two electrodes.

Detection efficiency in GG mode. Analytical properties of dual band devices performing in GG mode are characterized by their cooperating efficiency $(\psi_{g1}+\psi_{g2})/Pe$ and by the thickness (H_1+H_2) of the layer of solution entering the microchannel which is probed by the electrode assembly.[47] H_1 is the thickness of the solution layer analyzed by the first electrode. Its value is estimated from the upstream asymptote of the streamline which connects the downstream edge of the first electrode to the solution far upstream from the device (Figure 7A). All electroactive material carried by the upstream solution

in the section comprised between $Y = 0$ and $Y = H_1$ is borne to hit the first electrode. H_2 has the same meaning for the second electrode, i.e., all electroactive material carried by the upstream solution in the layer $H_1 < Y \leq H_2$ will hit the second electrode. As a result, H_1 and H_2 characterize the "in depth penetration" of each electrode activity and (H_1+H_2) describes to the same for the activity of the assembly. Note that H_2 depends on the placement of E2 versus E1 (Figure 7A). Corresponding values of $(H_1+H_2) / H$ and $(\psi_{g1}+\psi_{g2}) / \psi$ are reported in Figure 7B as a function of G, where H and ψ are respectively the probed solution thickness and the current that would apply for a single electrode of equivalent width $W = W_1+W_2$. When $G = 0$, the situation is necessarily similar to that of one electrode so that $H = H_1+H_2$ and $\psi = \psi_{g1}+\psi_{g2}$. When G increases, $(H_1+H_2) / H$ and $(\psi_{g1}+\psi_{g2}) / \psi$ increases towards limiting values achieved when $G > 10$. In fact, these variations display the specific transition from coupling to sequential regimes established above based on current variations. Under these conditions, numerical analyses establish that a relation exists between solution thickness and collection efficiency as evidenced previously in the case of a single electrode[47] (Figure 7C):

$$\frac{\left(\Psi_{g1}+\Psi_{g2}\right)}{Pe} = 3\left(H_1+H_2\right)^2 - 2\left(H_1+H_2\right)^3 \qquad (14)$$

This equation remains valid both in sequential and coupling regimes, *i.e.*, provided that diffusion does not proceed against the flow ($W_1Pe > 15$ and $W_2Pe > 15$) [47] and is characteristic of parabolic flows prevailing in microchannels. However, a dual assembly shows that the overall current densities at the electrodes are enhanced as shown in Figure 7B by $(\psi_{g1}+\psi_{g2}) / \psi > 1$. Therefore, one can deduce immediately that, thanks to the existence of the sequential regime, a dual assembly operated in GG mode gives rise to two main analytical advantages versus. a single electrode of identical length. Indeed on the one hand, the signal-to-noise ratio increases since the current densities achieved in this case are higher, in particular when the ratio $(W_1+W_2)/Pe$ is lower than unity (Figure 7D). On the other hand, because $(\psi_{g1}+\psi_{g2}) > \psi$, eq (14) and Figure 7C establish that $(H_1+H_2) > H$ as evidenced in Figure 7D. In other words, dual electrodes detectors "see" more deeply into solutions than detectors based on a single electrode of same surface area. The zone of sequential regime of the diagram in Figure 6 thus defines the optimal conditions in terms of (G,Pe) coordinates when the highest analytical efficiencies are achieved. In this context, one clearly foresees the analytical improvements given upon increasing the number of electrodes for optimizing amperometric detections within microchannels under steady state regime.[39]

CONCLUSION

This theoretical study based on numerical analyses allowed a complete quantitative evaluation of steady-state currents at dual microband electrodes embedded within a linear microchannel in which an analyte is transported by a parabolic flow. Generator-generator and generator-collector operating

modes were investigated allowing a detailed analysis of the current responses of the two electrodes. This allows identifying several types of interactions between electrodes according to the geometrical parameters of the devices and flow velocities considered. A very good agreement between simulations and experimental data was obtained over a wide range of operating conditions which validates a posteriori the experimental significance of all the predictions established in this work. When the gap distance is larger that the electrode widths, a zone diagram could be constructed to delineate the conditions where each type of interaction prevails. This diagram constitutes an important tool for optimizing specific electrochemical applications within microchannels taking advantage of dual microband electrodes assemblies. These results show already that the sequential regime provides the higher analytical efficiencies than single electrodes. In this context, the improvement given by using arrays of microelectrodes will be discussed in a further work.

Acknowledgements

This work has been supported in part by the CNRS (UMR 8640), the Ecole Normale Superieure, UPMC and the French Ministry of Research. The authors thank Prof. Y. Chen for their kind help in lithography and lift-off techniques.

APPENDIX

In sequential regime and under hydrodynamic conditions corresponding to Levich regime, currents ψ_{g1} and ψ_{g2}, are equal to:

$$\Psi_{g1} = 1.468\ W_1^{2/3} Pe^{1/3} \tag{A1}$$

$$\Psi_{g2} = 1.468\ W_2^{2/3} Pe^{1/3} C_h \tag{A2}$$

where C_h is the homogeneous concentration given by eq.(13).

ψ_{c2} is obtained from application of flux conservation:

$$\Psi_{c2} = \Psi - \Psi_{g2} \tag{A3}$$

where ψ is the current at a single electrode of width W_2 such as:

$$\Psi = 1.468\ W_2^{2/3} Pe^{1/3} \tag{A4}$$

Combination of eqs (A1), (A2), (A3), (A4) and (13) thus gives:

$$\Psi_{c2} = 1.468^2\ \left(W_1 W_2\right)^{2/3}\ Pe^{-1/3} \tag{A5}$$

Finally, one obtains in GG mode:

$$\frac{\Psi_{g2}}{\Psi_{g1}} = \left(\frac{W_2}{W_1}\right)^{2/3} C_h \tag{A6}$$

and in GC mode:

$$\frac{\Psi_{c2}}{\Psi_{g1}} = 1.468\ \left(\frac{W_2}{Pe}\right)^{2/3} \tag{A7}$$

Furthermore, combination of eqs (A1),(A3), (A4) affords:

$$\frac{\Psi_{c2}}{\Psi_{g1}} = \left(\frac{W_2}{W_1}\right)^{2/3} - \frac{\Psi_{g2}}{\Psi_{g1}} \tag{A8}$$

When $W = W_1 = W_2$, eqs (A6) and (A8) are equivalent to eqs (10) and (12).

REFERENCES

(1) Yi, C.; Qi, Z.; Li, C.-W.; Yang, J.; Zhao, J.; Yang, M. *Anal. Bioanal. Chem.* **2006**, *384*, 1259-1268.

(2) Dittrich, P. S.; Tachikawa, K.; Manz, A. *Anal. Chem.* **2006**, *78*, 3887-3907.

(3) Du, Y.; Wang, E. K. *J. Sep. Sci.* **2007**, *30*, 875-890.

(4) Anderson, J. L.; Ou, T. Y.; Moldoveanu, S. *J. Electroanal. Chem.* **1985**, *196*, 213-226.

(5) Bjorefors, F.; Strandman, C.; Nyholm, L. *Electroanalysis* **2000**, *12*, 255-261.

(6) Hayashi, K.; Iwasaki, Y.; Kurita, R.; Sunagawa, K.; Niwa, O. *Electrochem. Commun.* **2003**, *5*, 1037-1042.

(7) Goral, V. N.; Zaytseva, N. V.; Baeumner, A. J. *Lab Chip* **2006**, *6*, 414-421.

(8) Zhao, M.; Hibbert, D. B.; Gooding, J. J. *Anal. Chem.* **2003**, *75*, 593-600.

(9) Hayashi, K.; Iwasaki, Y.; Kurita, R.; Sunagawa, K.; Niwa, O.; Tate, A. *J. Electroanal. Chem.* **2005**, *579*, 215-222.

(10) Hashimoto, M.; Upadhyay, S.; Suzuki, H. *Biosens. Bioelectron.* **2006**, *21*, 2224-2231.

(11) Compton, R. G.; Stearn, G. M.; Unwin, P. R.; Barwise, A. J. *J. Appl. Electrochem.* **1988**, *18*, 657-665.

(12) Paixao, T. R. L. C.; Matos, R. C.; Bertotti, M. *Electrochim. Acta* **2003**, *48*, 691-698.

(13) Amatore, C.; Oleinick, A.; Svir, I.; Da Mota, N.; Thouin, L. *Nonlinear Analysis: Model. Contr.* **2006**, *11*, 345-365.

(14) Dayon, L.; Roussel, C.; Girault, H. H. *J. Proteome Res.* **2006**, *5*, 793-800.

(15) Zettersten, C.; Lomoth, R.; Hammarstrom, L.; Sjoberg, P. J. R.; Nyholm, L. *J. Electroanal. Chem.* **2006**, *590*, 90-99.

(16) Cooper, J. A.; Compton, R. G. *Electroanalysis* **1998**, *10*, 141-155.

(17) Fulian, Q.; Fisher, A. C.; Riley, D. J. *Electroanalysis* **2000**, *12*, 503-508.

(18) Amatore, C.; Pébay, C.; Servant, L.; Sojic, N.; Szunerits, S.; Thouin, L. *ChemPhysChem.* **2006**, *7*, 1322-1327.

(19) Ferrigno, R.; Josserand, J.; Brevet, P. F.; Girault, H. H. *Electrochim. Acta* **1998**, *44*, 587-595.

(20) Horii, D.; Atobe, M.; Fuchigami, T.; Marken, F. *Electrochem. Commun.* **2005**, *7*, 35-39.

(21) Paddon, C. A.; Atobe, M.; Fuchigami, T.; He, P.; Watts, P.; Haswell, S. J.; Pritchard, G. J.; Bull, S. D.; Marken, F. *J. Appl. Electrochem.* **2006**, *36*, 617-634.

(22) Aoki, K.; Tokuda, K.; Matsuda, H. *J. Electroanal. Chem.* **1985**, *195*, 229-249.

(23) Compton, R. G.; Gooding, J. J.; Sokirko, A. *J. Appl. Electrochem.* **1996**, *26*, 463-469.

(24) Wu, J.; Sansen, W. *Sensor. Actuat. A-Phys* **2002**, *97-98*, 68-74.

(25) Amatore, C.; Belotti, M.; Chen, Y.; Roy, E.; Sella, C.; Thouin, L. *J. Electroanal. Chem.* **2004**, *573*, 333-343.

(26) Wu, J.; Ye, J. *Lab. Chip* **2005**, *5*, 1344-1347.

(27) Wu, J.; Zhou, Q. L.; Liu, J.; Lou, Z. G. *Sensors* **2006**, *6*, 473-479.
(28) Amatore, C.; Chen, Y.; Sella, C.; Thouin, L. *Houille Blanche* **2006**, 60-64.
(29) Compton, R. G.; Coles, B. A.; Fisher, A. C. *J. Phys. Chem.* **1994**, *98*, 2441 - 2445.
(30) Compton, R. G.; Coles, B. A.; Gooding, J. J.; Fisher, A. C.; Cox, T. I. *J. Phys. Chem.* **1994**, *98*, 2446-2451.
(31) Amatore, C.; Sella, C.; Thouin, L. *J. Electroanal. Chem.* **2006**, *593*, 194-202.
(32) Aoki, K.; Tokuda, K.; Matsuda, H. *J. Electroanal. Chem.* **1977**, *79*, 49-78.
(33) Ou, T. Y.; Moldoveanu, S.; Anderson, J. L. *J. Electroanal. Chem.* **1988**, *247*, 1-16.
(34) Fisher, A. C.; Compton, R. G. *J. Appl. Electrochem.* **1991**, *21*, 208-212.
(35) Thompson, M.; Klymenko, O. V.; Compton, R. G. *J. Electroanal. Chem.* **2005**, *576*, 333-338.
(36) Paixao, T. R. L. C.; Richter, E. M.; Brito-Neto, J. G. A.; Bertotti, M. *J. Electroanal. Chem.* **2006**, *596*, 101-108.
(37) Roston, D. A.; Kissinger, P. T. *Anal. Chem.* **1982**, *54*, 429-434.
(38) Martin, R. S.; Gawron, A. J.; Lunte, S. M.; Henry, C. S. *Anal. Chem.* **2000**, *72*, 3196-3202.
(39) Amatore, C.; Da Mota, N.; Sella, C.; Thouin, L. *Anal. Chem.* **2008**, *80*, 4976-4985.
(40) Matsuda, H. *J. Electroanal. Chem.* **1968**, *16*, 153-164.
(41) Aoki, K.; Matsuda, H. *J. Electroanal. Chem.* **1978**, *94*, 157-163.
(42) Alden, J. A.; Compton, R. G. *J. Electroanal. Chem.* **1996**, *415*, 1-12.
(43) Amatore, C.; Oleinick, A.; Svir, I. *Electrochem. Commun.* **2004**, *6*, 1123-1130.
(44) Thompson, M.; Compton, R. G. *J. Electroanal. Chem.* **2005**, *583*, 318.
(45) Klymenko, O. V.; Oleinick, A. I.; Amatore, C.; Svir, I. *Electrochim. Acta* **2007**, *53*, 1100-1106.
(46) Amatore, C.; Klymendo, O. V.; Oleinick, A.; Svir, I. *Chem. Phys. Chem.* **2007**, *8*, 1870-1874.
(47) Amatore, C.; Da Mota, N.; Sella, C.; Thouin, L. *Anal. Chem.* **2007**, *79*, 8502-8510.
(48) Matthews, S. M.; Du, G. Q.; Fisher, A. C. *J. Solid State Electrochem* **2006**, *10*, 817-825.
(49) Maisonhaute, E.; White, P. C.; Compton, R. G. *J. Phys. Chem. B* **2001**, *105*, 12087-12091.
(50) Amatore, C.; Thouin, L.; Warkocz, J.-S. *Chem. Eur. J.* **1999**, *5*, 456-465.
(51) Arkoub, I. A.; Amatore, C.; Sella, C.; Thouin, L.; Warkocz, J.-S. *J. Phys. Chem. B* **2001**, *105*, 8694-8703.

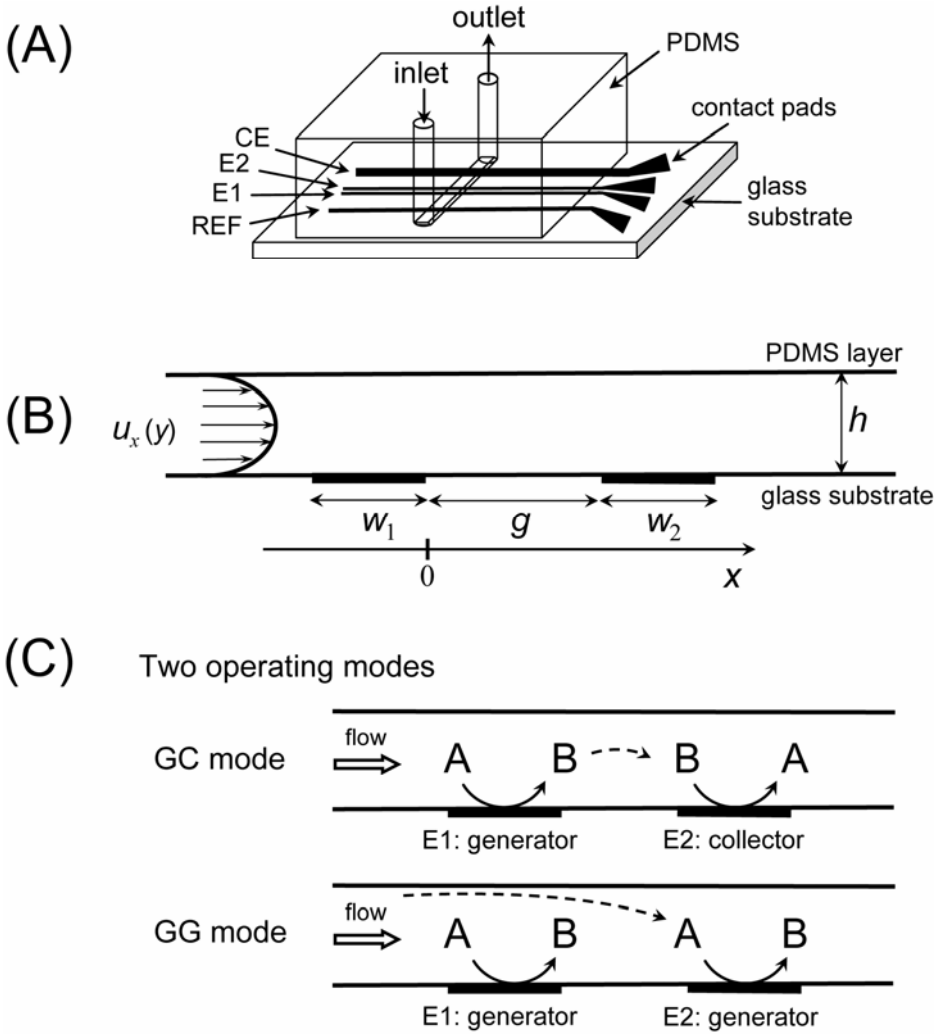

Figure 1: (A) 3D-schematic view of the microfluidic devices investigated in this work showing the relative positions of the two working electrodes (E1 and E2), pseudo-reference electrode (REF) and counter electrode (CE). (B) 2D-cross section of the microchannel with definition of geometrical parameters (w_1, w_2, g and h) and illustration of the parabolic profile of the flow velocity $u_x(y)$. (C) 2D-schemes describing the two operating modes at E1 and E2: generator-collector mode (GC) and generator-generator mode (GG). The solution present at the entrance of the microchannel contains only species A while the electrolytic product B is formed only at the electrodes.

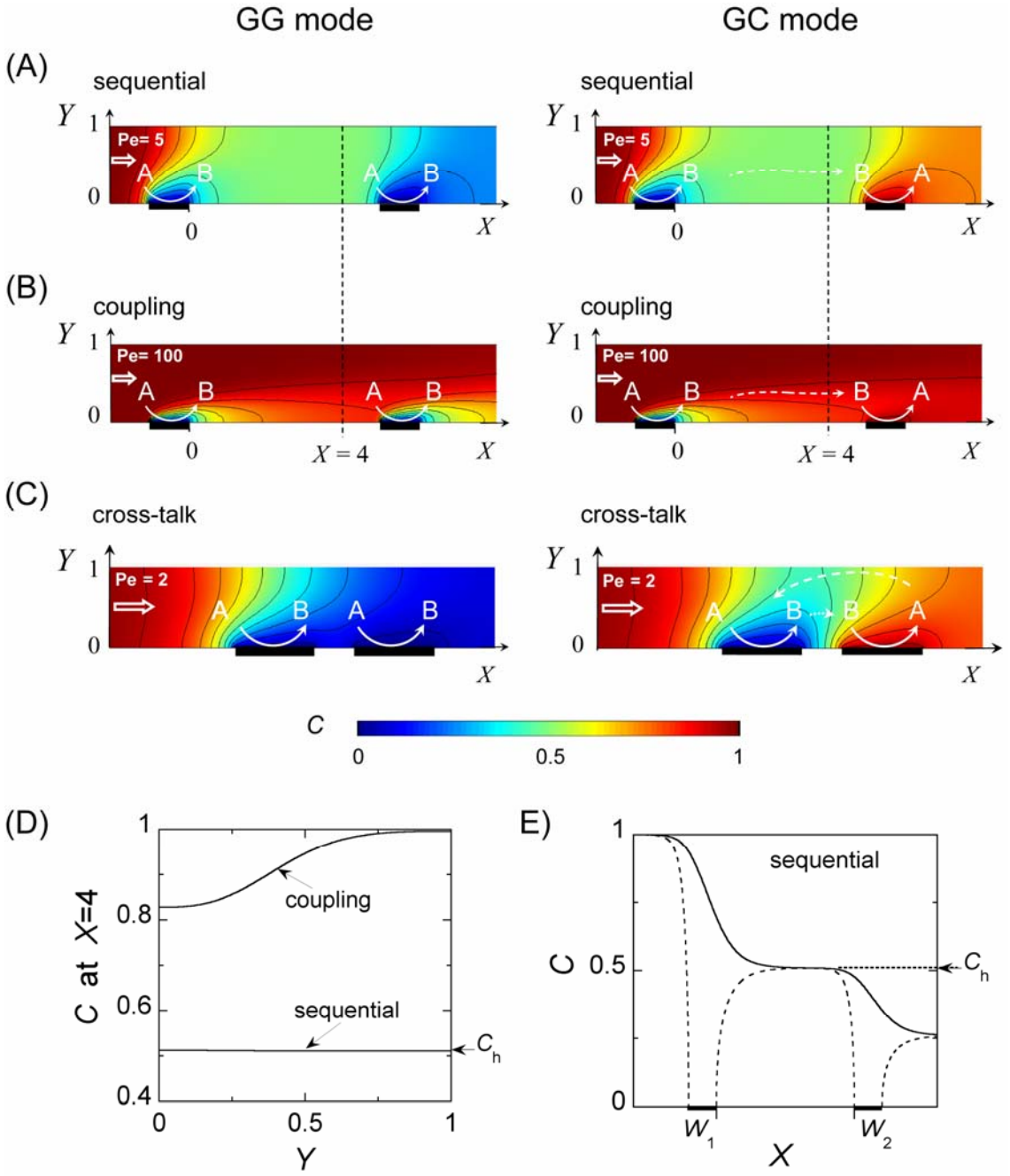

Figure 2: (A-C) Steady-state concentration profiles developing over a pair of microband electrodes ($W_1 = W_2 = 1$) operating in GG or GC modes: (A) sequential regime ($G = 5$ and $Pe = 5$), (B) coupling regime ($G = 5$ and $Pe = 100$) and (C) cross talk regime ($G = 0.5$ and $Pe = 2$). The solid curves superimposed to the colored charts represent 10 isoconcentration lines ranging from $C = 0.05$ to 0.95 in steps of 0.1. In (A) and (B), the Y scale is expanded twice. (D) Concentration profiles developing vertically across the microchannel section at $X = 4$ (i.e., corresponding to the vertical dashed lines in (A) and (B)) in the two limiting regimes. (E) Concentration profiles along the X-axis at $Y = 0$ (dashed line) and $Y = 1$ (solid line) for a GG operating mode. In (D) and (E), C_h is the homogeneous concentration reached between the two electrodes.

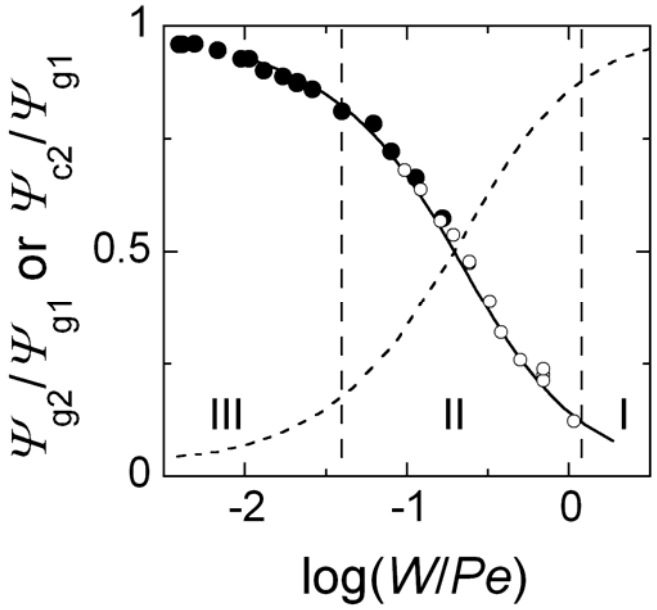

Figure 3: Variations of current ratios Ψ_{g2} / Ψ_{g1} (solid curve, GG mode) or Ψ_{c2} / Ψ_{g1} (dashed curve, GC mode) versus log(*W*/*Pe*) when a sequential regime prevails at a pair of microband electrodes of identical width $W = W_1 = W_2$. The curves are results of numerical simulations and the symbols the experimental data obtained in a GG mode: (●) $W = 0.8$, $G = 29$ and (○) $W = 9$, $G = 14$. The solid curve represents also the variation of C_h established previously[47] in zone I (thin layer regime), zone II (intermediate regime) and zone III (Levich regime).

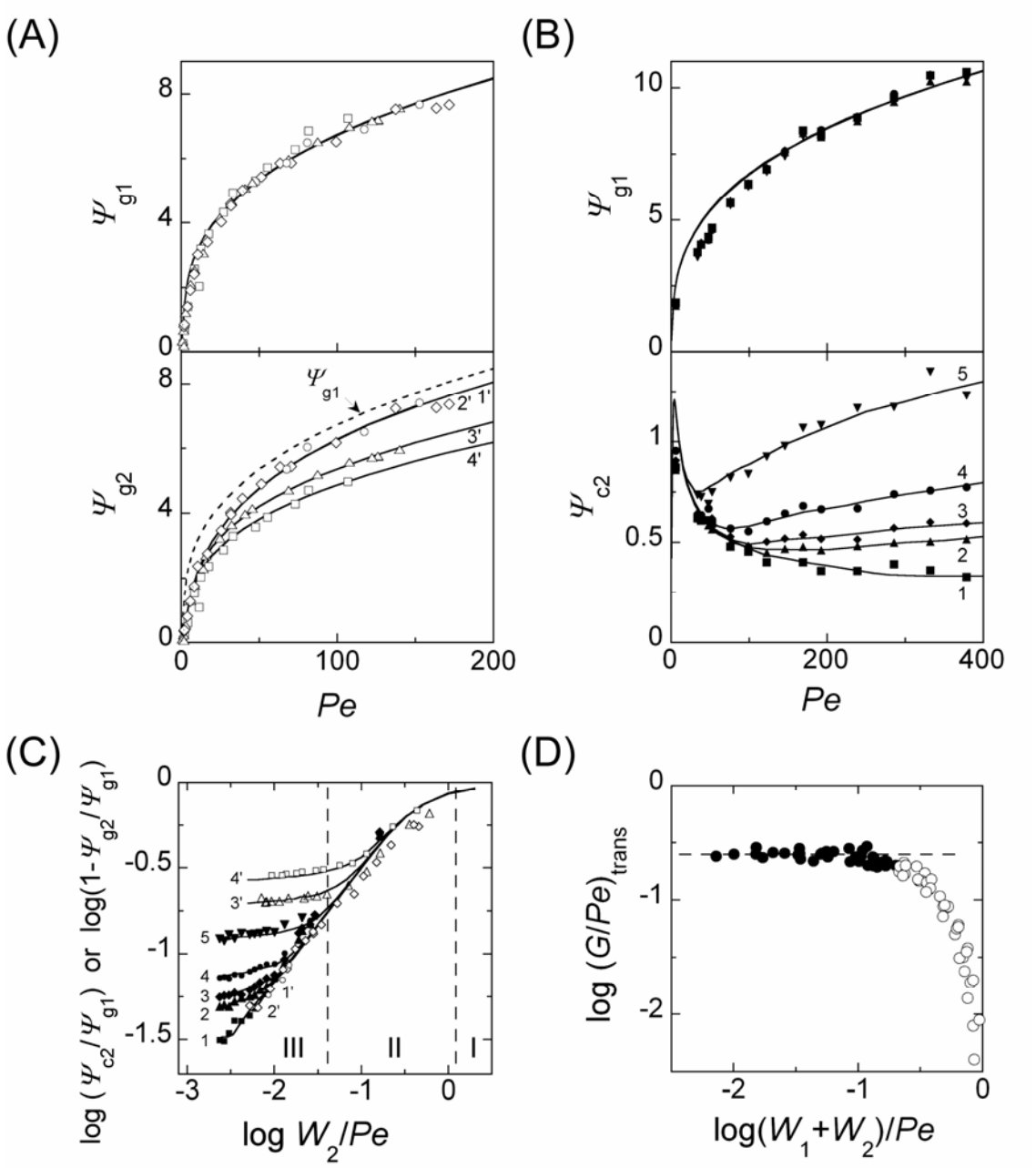

Figure 4: (A-B) Experimental (symbols) and simulated (solid curves) steady-state currents at a pair of microband electrodes as a function of *Pe* for various gap distances *G*. (A) GG mode (top: Ψ_{g1}; bottom: Ψ_{g2}) with $G = 150$ (○, 1'), 37.6 (◊, 2'), 2.35 (Δ, 3'), 1 (□, 4'). (B) GC mode (top: Ψ_{g1}; bottom: Ψ_{c2}) with $G = 76.5$ (■, 1), 28.8 (▲, 2), 23.5 (♦, 3), 14.7 (●, 4), 5.9 (▼, 5). In (A) and (B) $W_1 = W_2 = 1$. (C) Variations of $\log(\Psi_{c2} / \Psi_{g1})$ or $\log(1-\Psi_{g2} / \Psi_{g1})$ versus $\log(W_2/Pe)$ calculated from data in (A) and (B). Zones I, II, III represent those where the same regimes described in Figure 3 prevail. (D) Variation of $(G/Pe)_{trans}$ as a function of $(W_1+W_2)/Pe$ as predicted from simulations: (●) $(W_1+W_2) \leq G$ and (○) $(W_1+W_2) > G$. Values of $(G/Pe)_{trans}$ characterized the transition between sequantial and coupling regimes. The dashed line corresponds to $G/Pe = 0.25$.

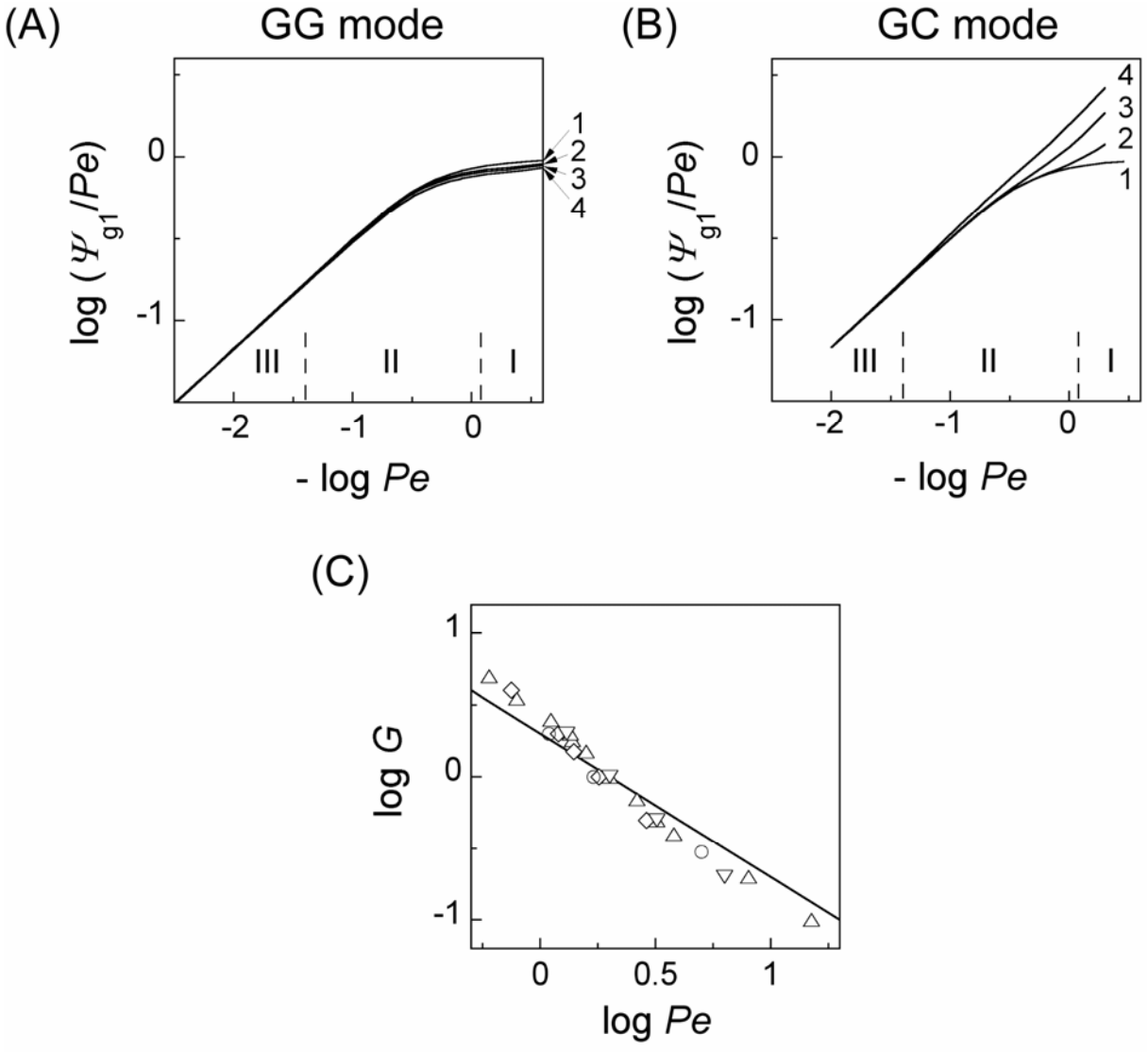

Figure 5: (A-B) Simulated variations of $\log(\Psi_{g1} / Pe)$ versus $-\log(Pe)$ at the upstream electrode E1 during GG mode (A) and GC mode (B) operations for various gap distances with $G > 5$ (1), $G = 2$ (2), $G = 0.5$ (3) and $G = 0.1$ (4). $W_1 = W_2 = 1$. Zones I, II, III represent those in which the regimes described in Figure 3 prevail when $W = 1$. (C) Variation of $\log G$ as a function of $\log Pe$ for maintaining the system at the same transition point between cross-talk and other regimes: $W_1 = W_2 = 1$ (Δ), $W_1 = W_2 = 5$ (◊), $W_1 = 1$ and $W_2 = 5$ (∇), $W_1 = 5$ and $W_2 = 1$ (○). The solid line corresponds to $GPe = 2$.

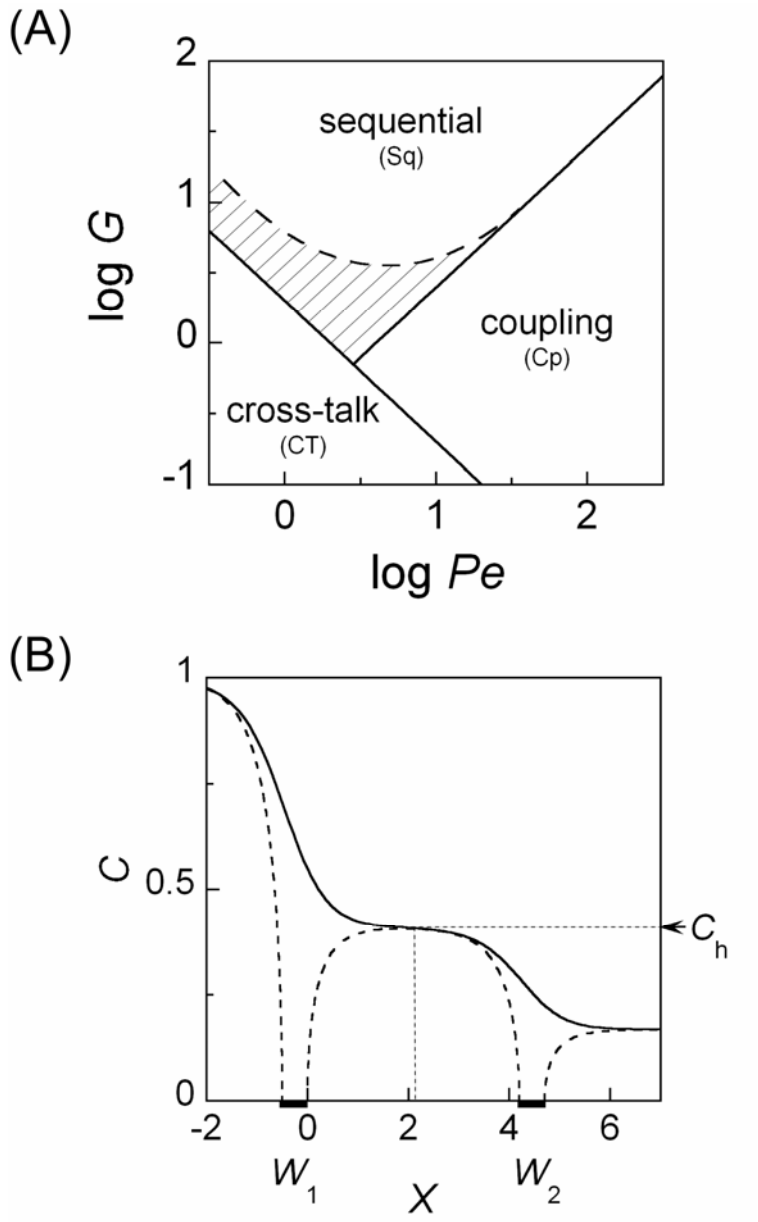

Figure 6: (A) Zone diagram describing the areas in a (*G*,*Pe*) space where the sequential, coupling and cross-talk regimes take place between pairs of microband electrodes when $(W_1+W_2) << G$. The solid lines represent the transitions established considering only current variations respectively for $G/Pe = 0.25$ (transition between sequential and coupling regimes, Figure 4D) and $GPe = 2$ (cross-talk, Figure 5C). The dashed curve corresponds to the transition evaluated from concentration profiles (note that the dashed area appears as a pure sequential regime on basis of current measurements only). (B) Concentration profiles along the *X*-axis at $Y = 0$ (dashed line) and $Y = 1$ (solid line) in GG mode for $W_1 = W_2 = 0.5$, $G = 4.2$ and $Pe = 2$, viz., at the limit between the hatched zone in A and that featuring the sequential regime.

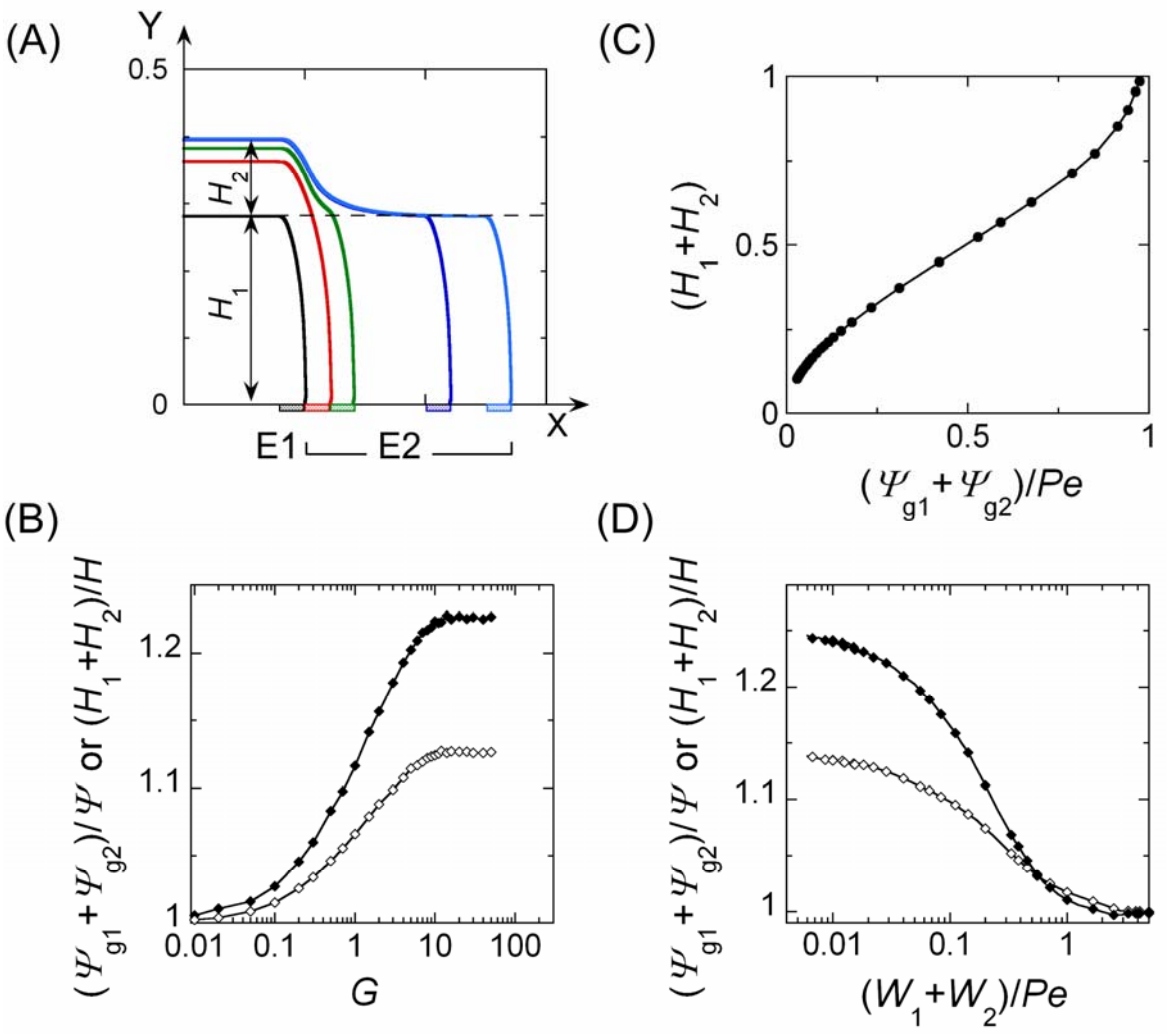

Figure 7: (A) Streamlines delineating the range of the solution passing in front of a GG assembly as a function of the placement of the second electrode. Each streamlines is linking the microchannel entrance to the downstream edge of each electrode. The streamline shown in black corresponds to electrode E1. The streamlines in color correspond to electrode E2 for different gap distances: $G = 0$ (red), 2 (green); 10 (dark blue) and 15 (blue). $Pe = 40$. (B) Simulated variation of (H_1+H_2) (symbols) versus $(\Psi_{g1}+\Psi_{g2}) / Pe$. The solid curve corresponds the predictions in eq (14). (C) Simulated variation of $(H_1+H_2) / H$ (◊) and $(\Psi_{g1}+\Psi_{g2}) / \Psi$ (♦) versus G with $W_1 = W_2 = W / 2 = 1$ and $Pe = 40$ for a GG operating mode. (D) Simulated variation of $(H_1+H_2) / H$ (◊) and $(\Psi_{g1}+\Psi_{g2}) / \Psi$ (♦) versus (W_1+W_2) with $W_1 = W_2 = W/2$, $Pe = 40$ and $G > 10$ for a GG operating mode.